The Journal of Experimental Biology 211, 280-287
Published by The Company of Biologists 2008
doi:10.1242/jeb.007641

Research article

An overview of a Lagrangian method for analysis of animal wake dynamics

Jifeng Peng[1] and John O. Dabiri[1,2,*]

[1]Bioengineering and [2]Graduate Aeronautical Laboratories, California Institute of Technology, Pasadena, CA 91125, USA

*Author for correspondence (e-mail: jodabiri@caltech.edu)

Accepted 22 May 2007

Summary

The fluid dynamic analysis of animal wakes is becoming increasingly popular in studies of animal swimming and flying, due in part to the development of quantitative flow visualization techniques such as digital particle imaging velocimetry (DPIV). In most studies, quasi-steady flow is assumed and the flow analysis is based on velocity and/or vorticity fields measured at a single time instant during the stroke cycle. The assumption of quasi-steady flow leads to neglect of unsteady (time-dependent) wake vortex added-mass effects, which can contribute significantly to the instantaneous locomotive forces. In this paper we review a Lagrangian approach recently introduced to determine unsteady wake vortex structure by tracking the trajectories of individual fluid particles in the flow, rather than by analyzing the velocity/vorticity fields at fixed locations and single instants in time as in the Eulerian perspective. Once the momentum of the wake vortex and its added mass are determined, the corresponding unsteady locomotive forces can be quantified. Unlike previous studies that estimated the time-averaged forces over the stroke cycle, this approach enables study of how instantaneous locomotive forces evolve over time. The utility of this method for analyses of DPIV velocity measurements is explored, with the goal of demonstrating its applicability to data that are typically available to investigators studying animal swimming and flying. The methods are equally applicable to computational fluid dynamics studies where velocity field calculations are available.

Key words: wake, vortex, force, locomotion, Lagrangian coherent structure, added mass, fluid dynamics.

Introduction

Vortices are thought to play an important role in the mechanisms of animal swimming and flying due to their prominence in the fluid surrounding the animal. For example, vortex formation has been identified as the key mechanism that enables many insects to generate sufficient lift in flight (Maxworthy, 1979; Ellington et al., 1996; Willmott et al., 1997; Sane, 2003). These animals rely on the stably attached leading-edge vortex created by the insect wing during flapping motions; the presence of this vortex greatly enhances the forces used to hover and maneuver. Although this leading-edge vortex mechanism is not as commonly observed in swimming animals, the vortices generated during aquatic locomotion also appear to affect thrust, maneuvering and propulsive efficiency, i.e. the ratio of useful work for locomotion to the total mechanical energy input (since the motion is typically unsteady, propulsive efficiency is non-zero). Many examples can be found in the swimming of medusae, amphibians, fishes, marine mammals, etc. (e.g. Drucker and Lauder, 1999; Wilga and Lauder, 2004; Bartol, 2005; Dabiri et al., 2005; Stamhuis and Nauwelaerts, 2005).

Most studies investigate momentum transfer from the animal to the fluid in the form of vortices, with the ultimate goal of quantifying locomotive forces and understanding the role of vortices in swimming and flying mechanisms. Indeed, the presence of vorticity, or the resulting circulation to be more precise, is necessary in steady locomotion (cf. Kutta–Joukowski theorem). However, vortices are not solely responsible for animal locomotion (Schultz and Webb, 2002). For example, Kanso et al. (Kanso et al., 2005) demonstrated that, in theory, vorticity/circulation need not be present at all in order for an articulated body to achieve unsteady locomotion [see Saffman (Saffman, 1967) for an original proof-of-concept]. If vorticity is not necessary for unsteady locomotion, then perhaps there exist circumstances in which it is also not sufficient to achieve that locomotion. And, if the presence of vorticity is not sufficient to achieve certain modes of locomotion, then it is not likely that a study of vorticity alone can deduce the locomotive forces in those cases. These fundamental issues (including the question of whether unsteady locomotion in air and water may have actually arisen in spite of the presence of vorticity) have received relatively little attention thus far.

When an animal moves through fluid, Newton's second and third laws together dictate that the locomotive force exerted by the fluid on the animal has a magnitude equal to the rate at which the animal imparts momentum to the fluid. To be sure, viscous dissipation and vorticity cancellation will reduce the efficiency of the momentum transfer process from 100 per cent, resulting in an 'information loss' in the record of locomotive dynamics contained in the wake. However, a simple viscous scaling argument shows that these effects are usually negligible on the time scale of individual stroke cycles. In particular, the distance δ over which viscosity will act during a single stroke of duration T_S is $\delta \approx (\nu T_S)^{1/2}$, where ν is the kinematic viscosity of the fluid (Rosenhead, 1963). Regions of opposite-signed vorticity (e.g. shed from the anterior and posterior edges of a fin or wing) must be within this distance $(\nu T_S)^{1/2}$ from each other in order to undergo vorticity cancellation and the associated information loss in the wake. For repeated swimming or flying motions at frequency f_S, the scaling is equivalently $\delta \approx (\nu/f_S)^{1/2}$. Hence, information loss in the wake becomes important

if the ratio $\delta/L \approx (\nu/f_s)^{1/2}/L$ is of the order of one or larger, where L is the characteristic length scale of the appendage [the reader should recognize this as effectively the inverse square root of the Reynolds number (cf. White, 1991)]. A 1 Hz swimming motion in water ($\nu \approx 10^{-2}$ cm^2 s^{-1}) corresponds to a characteristic viscous length scale δ of ~1 mm, which is substantially smaller than the length scales of most fish appendages (although not necessarily small for swimming micro-organisms). In air ($\nu \approx 10^{-1}$ cm^2 s^{-1}) at 1 Hz, $\delta \approx 3$ mm, which is also smaller than the length scales of most bird appendages. Insects may have appendage length scales of this order but will also operate at much higher frequencies, thereby reducing the length scale δ. Therefore, for the near-wake (vis-à-vis far downstream) studies of concern here in which the ratio δ/L is small, we will assume no information loss between the dynamics of the animal and the wake it generates.

The development of visualization and measurement techniques, especially digital particle image velocimetry (DPIV), has given researchers the ability to quantify kinematics and dynamics of the animal wake (e.g. Muller et al., 1997; Drucker and Lauder, 1999; Nauwelaerts et al., 2005; Spedding et al., 2003; Warrick et al., 2005). To interpret the wake measurements, several models have been proposed to estimate momentum transfer and evaluate locomotive forces. For example, locomotive forces experienced by the animal are calculated as the reaction to the momentum of vortex loops shed into the wake (e.g. Drucker and Lauder, 1999; Drucker and Lauder, 2001; Johansson and Lauder, 2004; Stamhuis and Nauwelaerts, 2005). In these cases, the momentum of the vortex is usually measured at the time instant when the vortex ring has just detached from the animal fin/wing. The time-averaged locomotive force over the stroke cycle is then determined by dividing the momentum of the shed vortex by the time duration of the stroke cycle. In other studies, the locomotive forces have been evaluated by examining the wake far downstream, which is equivalent to taking the time average of dynamics occurring at the site of force generation (e.g. Spedding et al., 2003; Walker, 2004).

Only time-averaged locomotive forces (vis-à-vis time-dependent forces) can be determined in the aforementioned studies because they implicitly assume that the flow is steady so that the vortex momentum can be determined from the distribution of vorticity alone. As noted above, spatial vorticity distribution is insufficient by itself to determine unsteady fluid dynamic forces; the velocity potential is needed as well (Saffman, 1992). Dabiri (Dabiri, 2005) suggested a connection between velocity potential and wake vortex added mass and expressed the vortex momentum based on the bulk motion of the vortex and its added mass. When a vortex, interacting with a swimming or flying appendage [e.g. during formation of the vortex by the appendage, or interaction with vortices formed upstream as in Liao et al. (Liao et al., 2003a; Liao et al., 2003b)], is accelerated through the surrounding fluid, it faces resistance due to the inertia of fluid surrounding the vortex that is brought into motion with the vortex. The inertia of this surrounding fluid in the direction of vortex motion is the source of the added mass. The governing fluid physics for wake vortex added mass is identical to that for solid body added mass (Dabiri, 2006), and in a steady flow the wake vortex added mass can be deduced solely from the distribution of vorticity (Krueger, 2001). However, in an unsteady flow this is no longer possible. Dabiri et al. (Dabiri et al., 2006) showed that unsteady vortex added-mass effects become important for flows in which the ratio:

$$\frac{SU_{\mathrm{V}i}}{\Gamma} > \frac{1}{1+c_{ii}}$$

(i.e. unsteady effects accelerate wake vortex propagation) or:

$$\frac{SU_{\mathrm{V}i}}{\Gamma} < \frac{1}{1+c_{ii}}$$

(i.e. unsteady effects retard wake vortex propagation). Here, Γ is the circulation of the wake vortex, S is the characteristic width of the vortex in the direction of propagation, $U_{\mathrm{V}i}$ is the velocity of the vortex in the i-direction, and c_{ii} is the vortex added-mass coefficient for unidirectional motion in the i-direction. The former case is common during wake vortex formation, whereas the latter case may occur upon stroke reversal if wake capture is observed. One must use care in interpreting this ratio for vortices in the far downstream wake, because a reduced ratio:

$$\frac{SU_{\mathrm{V}i}}{\Gamma} < \frac{1}{1+c_{ii}}$$

can also arise due to vortex breakdown and transition to turbulence in the wake, processes that are of secondary importance to the instantaneous locomotive dynamics.

Determination of wake vortex added mass in an unsteady flow depends critically on identification of the physical boundary of the vortex. Using a concept from dynamical systems called Lagrangian coherent structures (LCS), the boundary of the vortex in a wake can be determined by tracking fluid particles in the wake and searching for material lines that are separatrices, effectively partitioning flow regions with different dynamics (Haller, 2001; Shadden et al., 2006).

In this paper, we review a recently developed analytical framework to empirically deduce unsteady swimming and flying forces based on the measurement of velocity and vortex added mass in the animal wake. Given velocity field measurements in the wake, the vortex boundary can be determined and the momentum of the wake vortex and its added mass can be calculated, leading to a quantitative evaluation of instantaneous locomotive forces. The organization of this paper is as follows: (1) the LCS approach used to identify the boundary of the wake vortex is described; (2) the momentum of the wake vortex and locomotive forces are determined based on the morphology and kinematics of the vortex; (3) implementation of the method using 2-D velocity field data from DPIV measurements is explored.

Materials and methods

Vortex boundary identification

As in most fluid dynamics problems, the potential approaches for vortex boundary identification fall into one of two basic categories: Eulerian (i.e. fixed in space) or Lagrangian (i.e. moving with individual fluid particles). In most studies of animal vortex wakes, the vortex structure is determined from Eulerian data, using instantaneous vorticity or streamlines. For example, wake vortices have been previously identified by locating regions with vorticity above a given threshold (e.g. Drucker and Lauder, 1999; Drucker and Lauder, 2001; Stamhuis and Nauwelaerts, 2005). Few studies use streamlines to identify vortex structures in the animal wake; streamlines are able to give a clearly defined vortex boundary in a purely steady flow (e.g. Hill's spherical vortex) but are of less use in the highly unsteady flows characteristic of swimming and flying. A method of coordinate transformation has been previously developed to expand the utility of streamlines in time-dependent flow (Dabiri and Gharib, 2004), but its use is limited to unsteady cases where a single characteristic velocity can be identified in the wake, e.g. in the isolated vortex ring-dominated wakes generated by some jellyfish, squids and salps.

An alternative is to study the wake from a Lagrangian perspective. Instead of studying the instantaneous velocity/vorticity field, fluid particle trajectories are used as the fundamental variable. By following fluid particle trajectories, vortices tend to emerge from the wake as coherent structures since, at the Reynolds numbers of relevance to animal locomotion, fluid particles remain inside a vortex over long convective time scales relative to fluid particles outside the vortex (Provenzale, 1999). An exact criterion for defining vortex boundaries in unsteady flows was introduced in a series of papers by Haller (Haller, 2001; Haller, 2002; Haller, 2005); the boundaries are referred as Lagrangian coherent structures (LCS). Recently, an approach using the finite-time Lyapunov exponent field (FTLE) to locate LCS was developed (Shadden et al., 2005; Shadden et al., 2006). This FTLE approach is preferable because of its relative simplicity and wide compatibility with other methods used to locate LCS in time-dependent flows [e.g. hyperbolic time approach (Haller, 2001)].

In the present study, the aforementioned FTLE approach was used to determine vortex boundaries. Given a flow map $\mathbf{x}(t) \rightarrow \mathbf{x}(t+T)$, the FTLE is defined as:

$$\sigma_{t_0}^{T}(\mathbf{x}) = \frac{1}{|T|} \ln \left\| \frac{\delta \mathbf{x}(t_0+T)}{\delta \mathbf{x}(t_0)} \right\| . \quad (1)$$

The FTLE measures, for particle trajectories starting near $\mathbf{x}(t_0)$, the maximum linearized growth rate of the distance perturbation $\delta\mathbf{x}$ between adjacent fluid particles over the interval T, for trajectories starting near $\mathbf{x}(t_0)$. In other words, it characterizes the amount of fluid particle separation, or stretching, about the trajectory of point $\mathbf{x}$ over the time interval $[t_0, t_0+T]$. The LCS boundaries are defined by the local maxima, or ridges, of the FTLE field (Haller, 2001). They indicate regions in the flow with distinct dynamics, e.g. vortices, because fluid particle pairs straddling the vortex boundary separate faster than other arbitrary fluid particle pairs. This is illustrated in Fig. 1. Consider the two nearby fluid particles initially on opposite sides of the vortex boundary. The two fluid particles separate from each other much faster than other arbitrary fluid particle pairs for which the two particles lie on the same side of the boundary, thus giving ridges of high values in the corresponding FTLE field.

The mathematical derivation is briefly summarized in Appendix A; however, the reader is directed to the aforementioned papers for greater technical detail.

As a proof of the concept, an example of the FTLE analysis is shown in Fig. 2 (Shadden et al., 2006). A vortex ring is generated in a water tank by a piston that accelerates fluid from right to left through the open end of a cylinder. Velocity field data on the median symmetry plane of the vortex is taken by DPIV. The FTLE field is calculated for the moving vortex ring on this median symmetry plane. The analysis is carried out in both backward time and forward time. The ridges of high values of FTLE indicate the geometry of the LCS. Whereas the vortex geometry cannot be determined from inspection of the velocity field or the corresponding vorticity field, the entire vortex boundary is revealed by combining the forward- and backward-time LCS.

Momentum and locomotive force estimation

The momentum of the vortex wake consists of two components: the linear momentum of the fluid inside the vortex and the linear momentum of the fluid surrounding the vortex that is brought into motion as the vortex accelerates.

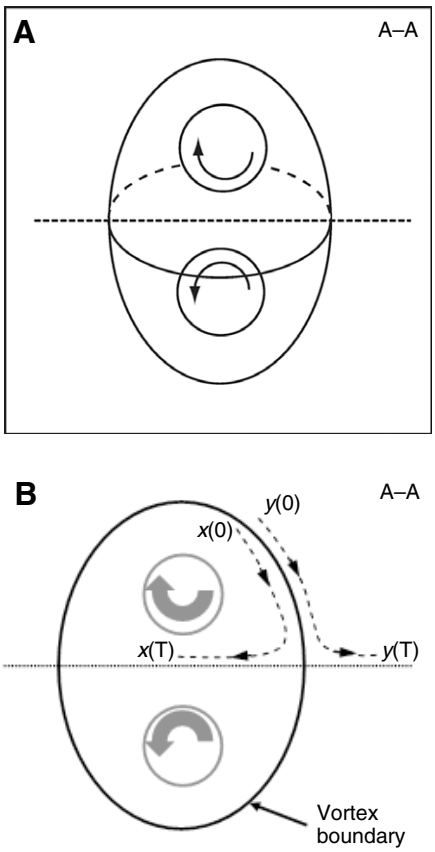

Fig. 1. Schematic diagram of a vortex boundary in a flow. (A) 3-D sketch of a vortex ring; (B) the vortex ring on its median-symmetry plane. Circles with inscribed arrows indicate vortex cores and their rotational sense. Two fluid particles close to but on different sides of the vortex boundary separate from each other faster than other arbitrary pairs of fluid particles, giving a larger value of the finite-time Lyapunov exponent field (FTLE) at the boundary. Adapted from Peng et al. (Peng et al., 2007).

The linear momentum of the fluid inside the vortex can be expressed as:

$$\mathbf{I}_{\text{inside}} = \rho \int_{V_v} \mathbf{U} dV , \quad (2)$$

where ρ is the density of the fluid, $\mathbf{U}$ is the velocity field inside the vortex, and V_V is the volume of the vortex, defined by the LCS as described in the previous section. If the wake vortex does not deform rapidly, the impulse of the fluid circulating inside the vortex can be simplified as:

$$\mathbf{I}_{\text{inside}} = \rho V_v \mathbf{U}_V , \quad (3)$$

where $\mathbf{U}_V$ is the velocity of the wake vortex center of mass. In this form, $\mathbf{I}_{\text{inside}}$ accounts for the momentum of the vortex body of volume V_V moving at a spatially averaged velocity $\mathbf{U}_V$.

The latter component of momentum arises from the added mass of the wake vortex and is identical to the added mass traditionally associated with fluid surrounding solid bodies in potential flow. The added mass is dependent on the shape of the body and can be determined using the Kirchhoff potential (see Appendix B for details). The boundary of a vortex ring (or, in 2-D, a vortex dipole) can be approximated by an ellipsoid (or, in 2-D, an infinitely long cylinder with an elliptical cross-section) whose added mass is given by an analytical expression (Lamb, 1932).

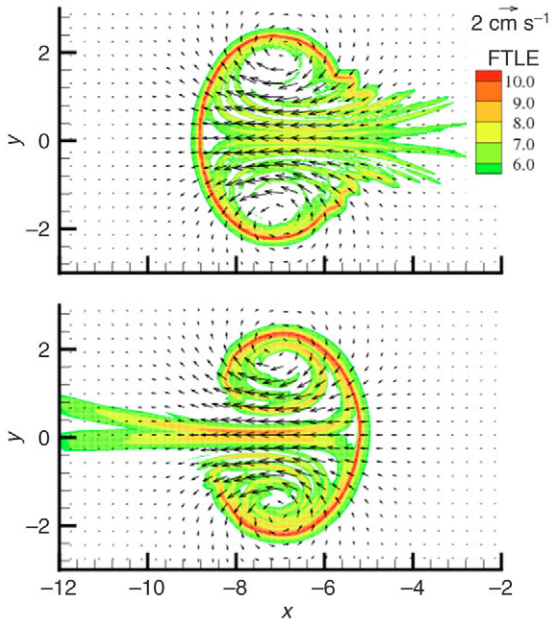

Fig. 2. Contour plots of FTLE fields calculated for a moving vortex ring (propagating from right to left across the page). Left: backward-time FTLE; right: forward-time FTLE. Adapted from Shadden et al. (Shadden et al., 2006).

Given the vortex added mass $\mathbf{M}_a$, the impulse of the wake vortex added mass can be expressed as:

$$\mathbf{I}_{\text{added mass}} = \mathbf{M}_a\mathbf{U}_V = \rho V_V \mathbf{C}\mathbf{U}_V \,, \tag{4}$$

where the added-mass coefficient $\mathbf{C}=\mathbf{M}_a/\rho V_V$ is the ratio of vortex added mass to the mass of the vortex itself. It should be mentioned here that the added mass $\mathbf{M}_a$ and its coefficient $\mathbf{C}$ are both tensor quantities (matrices). Depending on whether or not bulk rotational motion of the vortex (i.e. rotation of the principal axes of the vortex volume) is accounted for, the velocity $\mathbf{U}_V$ is either a 3×1 or 6×1 vector, and the added-mass tensor $\mathbf{M}_a$ is correspondingly a 3×3 or 6×6 matrix, respectively, with added-mass elements m_{ij} that relate acceleration in the ith direction to the resultant forces in the jth direction (where i and j can assume translation in x-, y- and z-axis directions in Cartesian coordinates, or rotation in the xy-, xz- and yz-planes: repeated subscripts m_{ii} do not indicate summation). If the added-mass effect from bulk rotational motion of the vortex is negligible, the added-mass tensor is a 3×3 matrix with non-zero components m_{ii} on the diagonal only, representing the added mass of the body associated with translational motion along each axis.

The total impulse $\mathbf{I}$ of the wake can then be simplified as:

$$\mathbf{I} = \rho V_V \mathbf{U}_V + \rho V_V \mathbf{C}\mathbf{U}_V \,. \tag{5}$$

By Newton's second and third laws, the locomotive force exerted by the fluid on the animal is equal and opposite to the rate at which the momentum $\mathbf{I}$ of the wake changes due to the interaction between the fluid and the animal:

$$\mathbf{F}_L = -\frac{\partial \mathbf{I}}{\partial t} = -\rho \frac{\partial}{\partial t}[(\mathbf{1}+\mathbf{C})V_V\mathbf{U}_V] \,. \tag{6}$$

Lagrangian wake analysis based on DPIV measurements

In this section, we discuss how to carry out the analyses described in the previous section by using a data set typically available to investigators studying animal swimming and flying: a time series of 2-D DPIV velocity fields [or equivalent computational fluid dynamics (CFD) data]. These velocity measurements are usually presented in a Eulerian frame, for which the velocity is defined at fixed locations in space and at a series of discrete instants in time. The locations in space at which velocity is measured usually form a structured grid with rectangular elements.

To determine the vortex boundary, the FTLE is calculated on a Cartesian grid defined in the region of the flow where the vortex exists. The flow map $\phi_{t_0}^{t_0+T}(\mathbf{x})$ at each node is calculated by integrating velocity data over each time step between two consecutive frames using a 4th-order Runge–Kutta integration algorithm. Since the velocity data are also discrete in space, a 3rd-order spatial interpolation is used to provide the necessary spatial resolution. Once all of the nodes are mapped from their initial positions at time $t=t_0$ to their final time $t=t_0+T$, the FTLE is determined on each node. The procedure is repeated for a range of times t_0 to provide a time series of FTLE fields showing the temporal evolution of the vortex structure. Positive and negative integration time intervals are used to determine forward- and backward-time FTLE fields, respectively, to locate repelling and attracting LCS (see Appendix A). The entire vortex boundary is given by combining the repelling and attracting LCS. Trials with a coarse grid might be used initially to determine the region of the flow where the LCS is located and the appropriate integration time T, before adopting a denser grid for higher spatial resolution calculation.

A color contour plot of the FTLE field and the application of a threshold are usually sufficient for the purpose of identifying the LCS. A more precise, mathematical approach to extract the LCS from the FTLE field is provided by Shadden (Shadden, 2006). There, the Hessian and the gradient of the FTLE field are calculated. Since the eigenvector of the Hessian corresponding to its minimum eigenvalue is tangent to the LCS and the gradient is normal to the LCS, a scalar field can be formed by taking the inner product of the two vector fields. LCS are extracted as zero-valued level sets.

We have developed an in-house MATLAB code to analyze experimental DPIV data or CFD data and to compute the corresponding FTLE field. The software, LCS MATLAB Kit version 1.0, can be downloaded at http://dabiri.caltech.edu/software.html. A more robust C-language software for this type of calculation is MANGEN, developed by F. Lekien and C. Coulliette. This package is also available online.

The vortex boundary is used to determine the volume V_V and the velocity $\mathbf{U}_V$ of the vortex. The components of the added-mass coefficient matrix $\mathbf{C}$ are also determined based on the vortex boundary information. Finally, the locomotive force at each time step can be determined according to Eqn 6 rewritten in a finite-difference form:

$$\mathbf{F}_L(t_j) = -\frac{\rho\{[\mathbf{1}+\mathbf{C}(t_{j+1})]V_V(t_{j+1})\mathbf{U}_V(t_{j+1}) - [\mathbf{1}+\mathbf{C}(t_j)]V_V(t_j)\mathbf{U}_V(t_j)\}}{\Delta t} \,. \tag{7}$$

It should be noted that the methods in the previous two sections are developed for general 3-D flows. For most animal wake studies, only 2-D velocity field data are available. The 2-D vortex boundary can be determined without difficulties. However, a 3-D approximation of the vortex structure is required when the vortex volume and its added-mass coefficient are calculated. For example, the volume and added mass of a 3-D vortex ring are quite different from those of a 2-D vortex dipole, though their cross-sections on the median plane can be similar. The 3-D vortex structures can be

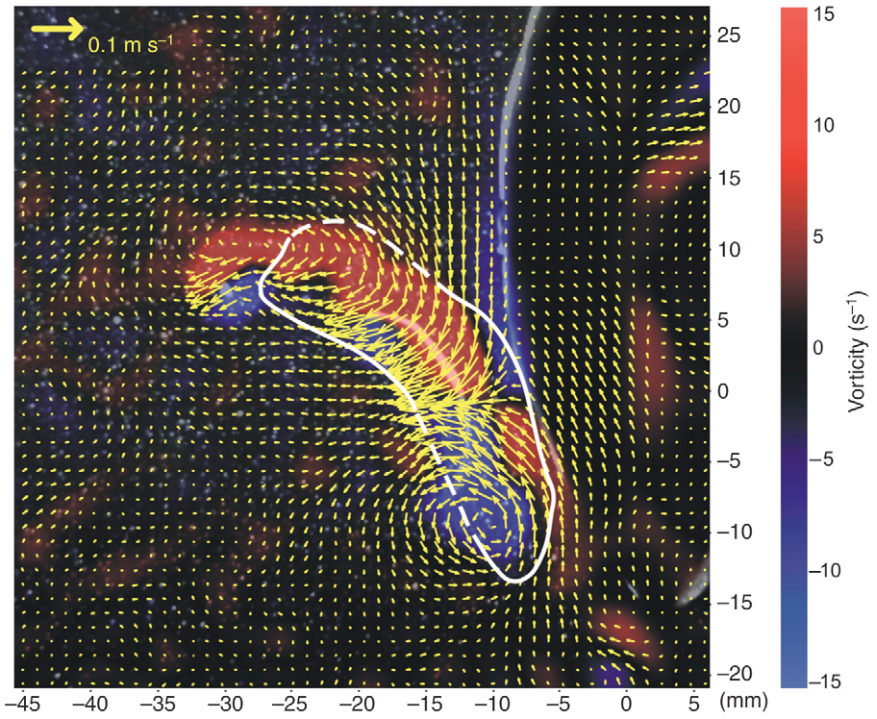

Fig. 3. The boundary of the vortex derived from Lagrangian coherent structures (LCS). The left solid line shows the attracting LCS from backward FTLE calculation while the right solid line shows the repelling LCS from forward FTLE calculation. Broken lines are spline lines connecting the LCS. The fin (curved with high brightness inside the lines) can be seen embedded inside the vortex. The attracting and repelling LCS do not intersect to give the entire vortex boundary due to the limitation in integration time *T*. Adapted from Peng et al. (Peng et al., 2007).

approximated by assuming the existence of two planes of spatial symmetry in the vortex, or by taking simultaneous DPIV measurements in multiple planes of the flow.

Results

Some results from an analysis of the wake generated by a bluegill sunfish pectoral fin (Peng et al., 2007) are shown here for illustration. The repelling and attracting LCS (see Appendix A) in the wake are shown in Fig. 3, superimposed on the velocity and vorticity fields. The evolution of the vortex boundary is shown in Fig. 4. These boundaries are assumed to lie on a symmetry plane. Another symmetry plane is assumed to exist normal to this first plane and equidistant from the vortex cores. The 3-D vortex structure is approximated based on this assumption of two planes of spatial symmetry. The vortex volume V_V and the velocity $\mathbf{U}_V$ together with the added-mass coefficient matrix $\mathbf{C}$ can then be determined and the locomotive forces evaluated. The results for the locomotive forces are shown in Fig. 5. Since two components of velocity $\mathbf{U}_V$ are known, forces in two directions (i.e. lateral and vertical) can be determined.

Discussion and conclusions

In this paper we have reviewed a framework for combining traditional DPIV measurements with a new class of Lagrangian analysis tools to analyze animal vortex wakes. The Lagrangian analysis provides clearly defined vortex boundaries in unsteady flows, a capability not offered by Eulerian analysis based on instantaneous vorticity or velocity fields. The information regarding the animal wake vortex boundary enables the determination of vortex added mass, which is a key component of locomotive forces in unsteady wakes. Using this framework, instantaneous forces, rather than time-averaged forces over a stroke cycle, can be determined. These instantaneous forces dictate important dynamics of locomotion such as the trajectory, speed and efficiency of swimming and flying.

As revealed in the example of sunfish pectoral fin wake, the fin is embedded within this wake vortex structure. Since it is known that the vortex is attached to the fin, this result suggests that the dynamical effect of the attached wake vortex on locomotion is to replace the real animal fin with an ‘effective appendage’, whose kinematics are determined by the external forces acting on it, e.g. the force the fish exerts to move the fin through the water in the example above. Furthermore, in the limit of irrotational, inviscid flow the ‘effective appendage’ reduces to the fin itself, and the only dynamical contribution for locomotion comes from the added mass of the fin. Thus, the ‘effective appendage’ concept provides a bridge between theoretical studies of locomotion in inviscid flows (e.g. Kanso et al., 2005) and the dynamics of real animals.

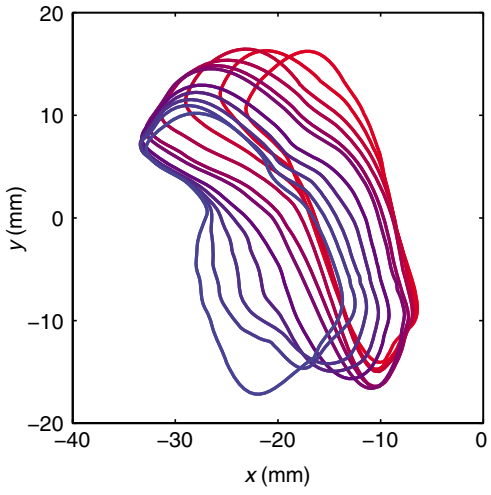

Fig. 4. Time evolution of the vortex boundary. Vortex boundaries at 11 different time instances are plotted from red (*t*=0 ms) to blue (*t*=300 ms) with a time interval of 30 ms. Adapted from Peng et al. (Peng et al., 2007).

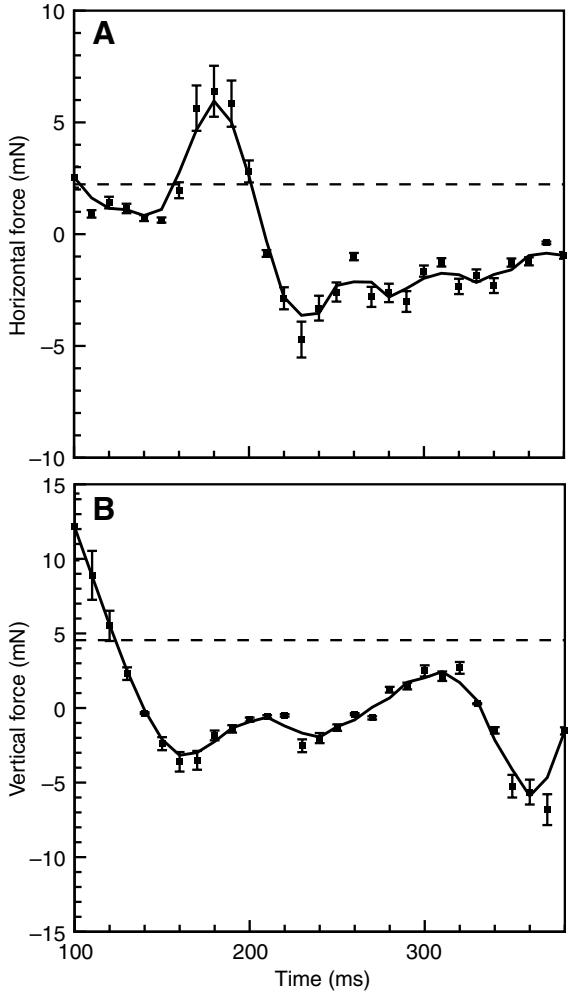

Fig. 5. The locomotive force in (A) the horizontal and (B) the vertical directions. Squares: calculated locomotive forces. Error bars indicate uncertainty from measurement and evaluation. Solid line: spline fitting of the data. Note that due to limitations on integration time, these plots are based on the first 400 ms of a 600 ms fin beat cycle. Adapted from Peng et al. (Peng et al., 2007).

Significant discrepancies can exist between the vortex boundary dictated by LCS and the spatial distribution of vorticity in the flow (e.g. Fig. 3). There are two primary sources for this disagreement. First, viscous diffusion occurring at these finite Reynolds numbers enables vorticity to cross the flow boundaries defined by the LCS, even when these boundaries form perfect barriers to fluid transport. A similar effect has been observed in studies of isolated vortex rings (Dabiri and Gharib, 2004; Shadden et al., 2006), and in the kinematics of boundary layer vorticity that defines 'displacement thickness' in steady flows (Rosenhead, 1963). The second and probably more dominant effect is that of appendage rotation, e.g. the anteroventral rotation of the sunfish pectoral fin during its downstroke. Haller (Haller, 2005) has shown that in flows with global rotation, the vorticity field can be a poor indicator of vortex boundaries. Hence, in these unsteady flows it is possible to lose a correlation between the wake vortex boundary dictated by the LCS and the spatial distribution of vorticity. The dynamical effect of vorticity external to the LCS is a topic of ongoing study.

If the entire animal is located inside the LCS, then the locomotive force is also internal to the LCS. In this case, the LCS can be treated using deformable body theory (Miloh and Galper, 1993) (cf. Eqn 5 and 6 above):

$$\mathbf{I} = \rho \int_{V_\mathrm{v}} \mathbf{U} \mathrm{d}V + \rho V_\mathrm{V} \mathbf{C} \mathbf{U}_\mathrm{V} = \text{constant} \ . \tag{8}$$

Assuming that the absolute velocity $\mathbf{U}$ of a fluid element in the volume of interest V_V can be expressed as the sum of the velocity of the center of mass $\mathbf{U}_\mathrm{V}$ and the velocity of that element relative to the center of mass $\mathbf{U}_\mathrm{d}$, i.e. $\mathbf{U}=\mathbf{U}_V+\mathbf{U}_\mathrm{d}$, Eqn 8 can be rewritten as:

$$\rho \int_{V_\mathrm{v}} \mathbf{U}_\mathrm{V} \mathrm{d}V + \rho V_\mathrm{V} \mathbf{C} \mathbf{U}_\mathrm{V} + \rho \int_{V_\mathrm{v}} \mathbf{U}_\mathrm{d} \mathrm{d}V = \text{constant} \tag{9}$$

$$\rho(\mathbf{1}+\mathbf{C}) V_\mathrm{V} \mathbf{U}_\mathrm{V} = \rho \int_{V_\mathrm{v}} \mathbf{U}_\mathrm{d} \mathrm{d}V = \text{constant} \ . \tag{10}$$

Applying Gauss's theorem to the volume integral in Eqn 10,

$$\rho \int_{V_\mathrm{v}} \mathbf{U}_\mathrm{d} \mathrm{d}V + \rho \int_{V_\mathrm{v}} \nabla \phi_\mathrm{d} \mathrm{d}V = \rho \int_{S_\mathrm{v}} \phi_\mathrm{d} \mathbf{n} \mathrm{d}S \ , \tag{11}$$

where ϕ_d is called the deformation potential (Miloh and Galper, 1993). The surface integral in Eqn 11 can be considered the fluid impulse (i.e. momentum) caused by the deformation $\mathbf{U}_\mathrm{d}$ on the surface of the wake vortex (now more loosely defined since S_V encloses the entire animal). Thus:

$$\rho(\mathbf{1}+\mathbf{C}) V_\mathrm{V} \mathbf{U}_\mathrm{V} + \mathbf{q} = \text{constant} \ , \tag{12}$$

where

$$\mathbf{q} = \rho \int_{V_\mathrm{v}} \mathbf{U}_\mathrm{d} \mathrm{d}V \tag{13}$$

is the fluid impulse generated by the deformation of the vortex body. Eqn 13 shows that the change of the total momentum of the LCS is equal to the fluid potential caused by the deformation of the LCS. This can be used to predict the trajectory of animals that swim by using undulatory motions of the entire body, e.g. jellyfish, whose entire body has been found to be enclosed by the forward- and backward-time LCS in our ongoing studies (Peng and Dabiri, 2007).

When the present analytical framework is applied to 3-D measurements, it can give much more accurate force estimates than in 2-D studies. With 3-D DPIV data, the boundary of the vortex can be determined directly instead of being approximated. The volume and added mass of the vortex can then be accurately quantified without making assumptions on the vortex structure. Identification of 3-D vortex boundaries would also enable evaluation of the effect of rotational added mass, which is neglected in the present study. Although 3-D flow visualization and measurement techniques have been developed and implemented (e.g. Pereira et al., 2000), they are not yet in use in studies of animal swimming and flying. In the meantime, the approach described here can be used to interpret 2-D DPIV measurement data already available to most researchers in the field. Estimation of instantaneous, unsteady locomotive forces can be made from these 2-D DPIV data, as shown in the example above. A potential improvement using current 2-D DPIV is simultaneous data collection in multiple perpendicular planes,

which can give additional 2-D geometric information regarding the 3-D vortex structure.

At this juncture, it is fair to ask how closely the estimates that are currently deduced from 2-D measurements – both in the present work and elsewhere in this field of study – agree with the 'correct' answer. Validation using numerically defined canonical flow fields is the goal of an ongoing study. Validation within the context of animal swimming would be difficult at present since it is not yet possible to simulate fully coupled fluid-structure dynamics of self-propelled animals where the body motion (e.g. flow-induced fin deformation) is solved iteratively rather than being fixed or prescribed *a priori*. Comparison with experimental measurements is also difficult in the absence of instantaneous fluid dynamic measurements (velocity field, forces and moments) that can be made simultaneously with recordings of instantaneous body dynamics. Until then, we can only achieve agreement amongst the various methods for force estimation. Recent results (e.g. Peng et al., 2007) suggest that the instantaneous force estimation techniques described here are compatible with time-averaged forces deduced from traditional vorticity studies and with qualitative observations of animal body dynamics.

Appendix A

FTLE calculation

Given a time-dependent velocity field $\mathbf{u}(\mathbf{x},t)$, the trajectory of a fluid particle $\mathbf{x}(t)$ can be determined by the ordinary differential equation:

$$\dot{\mathbf{x}}(t) = \mathbf{u}[\mathbf{x}(t),t] \ , \tag{A1}$$

with given initial conditions. The flow map, which maps fluid particles from their initial location at time t_0 to their location at time t_0+T can be expressed as:

$$\phi_{t_0}^{t_0+T}(\mathbf{x}) : \mathbf{x}(t_0) \rightarrow \mathbf{x}(t_0+T) \ , \tag{A2}$$

where $\phi_{t_0}^{t_0+T}(\mathbf{x})=\mathbf{x}(t_0+T)$ describes the current location of a fluid particle advected from the location $\mathbf{x}(t_0)$ at time t_0 after a time interval T. A given infinitesimal perturbation $\delta\mathbf{x}_0$ at time t_0 is transformed to $\delta\mathbf{x}$ by the relation:

$$\delta\mathbf{x} = \nabla\phi_{t_0}^{t_0+T}(\mathbf{x})\delta\mathbf{x}_0 \ , \tag{A3}$$

where $\nabla\phi_{t_0}^{t_0+T}(\mathbf{x})$ is the deformation gradient tensor and is defined by:

$$\nabla\phi_{t_0}^{t_0+T}(\mathbf{x}) = \frac{\mathrm{d}\phi_{t_0}^{t_0+T}(\mathbf{x})}{\mathrm{d}\mathbf{x}} \ . \tag{A4}$$

The magnitude of the perturbation is given by:

$$\|\delta\mathbf{x}\| = \sqrt{\langle\delta\mathbf{x}_0, [\nabla\phi(\mathbf{x})]^*\nabla\phi(\mathbf{x})\delta\mathbf{x}_0\rangle} \ , \tag{A5}$$

where $[\ ]^*$ denotes the transpose of matrix $[\ ]$. The symmetric matrix:

$$\Delta = [\nabla\phi_{t_0}^{t_0+T}(\mathbf{x})]^*\nabla\phi_{t_0}^{t_0+T}(\mathbf{x}) \tag{A6}$$

is the Cauchy–Green deformation tensor.

Let $\lambda_{max}(\Delta)$ be the maximum eigenvalue of the Cauchy–Green deformation tensor. Note from Eqn A5 that $[\lambda_{max}(\Delta)]^{1/2}$ gives the maximum stretching of $\mathbf{x}_0$ [i.e. the maximum separation of fluid particle pairs initially located at $\mathbf{x}(t_0)$] when $\mathbf{x}_0$ is aligned with the eigenvector associated with $\lambda_{max}(\Delta)$; hence,

$$\|\delta\mathbf{x}\|_{max} = \sqrt{\lambda_{max}(\Delta)}\ \|\delta\mathbf{x}_0\| \ . \tag{A7}$$

Introducing the finite-time Lyapunov exponent $\sigma_t^T(\mathbf{x})$:

$$\sigma_{t_0}^T(\mathbf{x}) = \frac{1}{|T|}\ \ln\ \sqrt{\lambda_{max}(\Delta)} = \frac{1}{|T|}\ \ln\left\|\frac{\delta\mathbf{x}(T)}{\delta\mathbf{x}(0)}\right\| \ , \tag{A8}$$

it measures the maximum linearized growth rate of the perturbation $\delta\mathbf{x}$ over the interval T, for trajectories starting near $\mathbf{x}(t_0)$. In other words, it characterizes the amount of fluid particle separation, or stretching, about the trajectory of point $\mathbf{x}$ over the time interval $[t_0,t_0+T]$.

It is important to note that though the FTLE $\sigma_t^T(\mathbf{x})$ is a function of position variable $\mathbf{x}$ and time t, it is thought of as a Lagrangian quantity since it is derived from fluid particle trajectories over the time interval $I=[t,t+T]$. The absolute value $|T|$ is used instead of T in Eqn A8 because FTLE can be computed for $T>0$ and $T<0$. The material line is called a repelling LCS ($T>0$) over the time interval I if infinitesimal perturbations away from this line grow monotonically under the linearized flow. The material line is called an attracting repelling LCS ($T<0$) if it is a repelling LCS over I in backward time.

The integration time $|T|$ is chosen according to the particular flow being analyzed. If a smaller integration time is used, then less of the boundary is revealed, whereas if a longer integration time is used, more of the boundary is revealed (i.e. relative differences in fluid particle behavior become more apparent when observed over longer periods of time). Generally, if the integration time $|T|$ is sufficiently long, the repelling and the attracting LCS usually intersect to give the boundary of the vortex [in cases where a vortex is known to be present; cf. Fig. 6 in Shadden et al. (Shadden et al., 2006)]. A larger integration time $|T|$ also gives LCS with higher spatial resolution. However, the choice of $|T|$ is sometimes limited in practice by the availability of data.

Appendix B

Added-mass calculation

For a vortex of arbitrary, possibly irregular shape, the added mass can be determined by using the Kirchhoff potential:

$$\mathbf{M}_a = -\rho\int_{S_v}\Phi\otimes\mathbf{n}\mathrm{d}S \ , \tag{B1}$$

where ρ is the fluid density, Φ is the Kirchhoff potential for steady translational motion of the vortex, $\mathbf{n}$ is the outward normal unit vector to the surface, and the symbol $\otimes$ represents a tensor product of two vectors. The integral is calculated on the entire surface of the body S_v. The components of Kirchhoff potential Φ are solutions of the Laplace equation whose gradient tends to zero at infinity and satisfies the boundary condition:

$$\frac{\partial\Phi}{\partial n} = \mathbf{n} \ . \tag{B2}$$

From Eqns B1 and B2 it can be seen that the added mass $\mathbf{M}_a$ depends solely on the shape of the wake vortex and not on its motion.

The authors thank C. P. Ellington and J. L. van Leeuwen for organizing the conference session in which this paper was originally presented in August 2006; M. S. Gordon for comments on the manuscript; and G. L. Brown, J. E. Marsden and P. Moin for enlightening discussions. The authors are also grateful to the anonymous referee for valuable suggestions that have led to several improvements in the manuscript. This research is funded by a grant from the Ocean Sciences Division, Biological Oceanography Program at NSF (OCE 0623475) to J.O.D.

References

Bartol, I. K. (2005). Body-induced vortical flows: a common mechanism for self-corrective trimming control in boxfishes. *J. Exp. Biol.* **208**, 327-344.

Dabiri, J. O. (2005). On the estimation of swimming and flying forces from wake measurements. *J. Exp. Biol.* **208**, 3519-3532.

Dabiri, J. O. (2006). Note on the induced Lagrangian drift and added-mass of a vortex. *J. Fluid Mech.* **547**, 105-113.

Dabiri, J. O. and Gharib, M. (2004). Fluid entrainment by isolated vortex rings. *J. Fluid Mech.* **511**, 311-331.

Dabiri, J. O., Colin, S. P., Costello, J. H. and Gharib, M. (2005). Flow patterns generated by oblate medusan jellyfish: field measurements and laboratory analyses. *J. Exp. Biol.* **208**, 1257-1265.

Dabiri, J. O., Colin, S. P. and Costello, J. H. (2006). Fast-swimming jellyfish exploit velar kinematics to form an optimal vortex wake. *J. Exp. Biol.* **209**, 2025-2033.

Drucker, E. G. and Lauder, G. V. (1999). Locomotor forces on a swimming fish: three-dimensional vortex wake dynamics quantified using digital particle image velocimetry. *J. Exp. Biol.* **202**, 2393-2412.

Drucker, E. G. and Lauder, G. V. (2001). Wake dynamics and fluid forces of turning maneuvers in sunfish. *J. Exp. Biol.* **204**, 431-442.

Ellington, C. P., van den Berg, C., Willmott, A. P. and Thomas, A. L. R. (1996). Leading-edge vortices in insect flight. *Nature* **384**, 626-630.

Haller, G. (2001). Distinguished material surfaces and coherent structures in three-dimensional fluid flows. *Physica D* **149**, 248-277.

Haller, G. (2002). Lagrangian coherent structures from approximate velocity data. *Phys. Fluids A* **14**, 1851-1861.

Haller, G. (2005). An objective definition of a vortex. *J. Fluid Mech.* **525**, 1-26.

Johansson, L. C. and Lauder, G. V. (2004). Hydrodynamics of surface swimming in leopard frogs (*Rana pipiens*). *J. Exp. Biol.* **207**, 3945-3958.

Kanso, E., Marsden, J. E., Rowley, C. W. and Melli-Huber, J. B. (2005). Locomotion of articulated bodies in a perfect fluid. *J. Nonlinear Sci.* **15**, 255-289.

Krueger, P. S. (2001). The significance of vortex ring formation and nozzle exit over-pressure to pulsatile jet propulsion. PhD thesis, California Institute of Technology, USA.

Lamb, H. (1932). *Hydrodynamics*. Cambridge: Cambridge University Press.

Liao, J. C., Beal, D. N., Lauder, G. V. and Triantafyllou, M. S. (2003a). The Kármán gait; novel kinematics of rainbow trout swimming in a vortex street. *J. Exp. Biol.* **206**, 1059-1073.

Liao, J. C., Beal, D. N., Lauder, G. V. and Triantafyllou, M. S. (2003b). Fish exploiting vortices decrease muscle activity. *Science* **302**, 1566-1569.

Maxworthy, T. (1979). Experiments on the Weis-Fogh mechanism of lift generation by insects in hovering flight. 1. Dynamics of the fling. *J. Fluid Mech.* **93**, 47-63.

Miloh, T. and Galper, A. (1993). Self-propulsion of general deformable shapes in a perfect fluid. *Proc. R. Soc. Lond. A Math. Phys. Sci.* **442**, 273-299.

Muller, U. K., Van den Heuvel, B. L. E., Stamhuis, E. J. and Videler, J. J. (1997). Fish foot prints: morphology and energetics of the wake behind a continuously swimming mullet (Chelon labrosus risso). *J. Exp. Biol.* **200**, 2893-2906.

Nauwelaerts, S., Stamhuis, E. J. and Aerts, P. (2005). Propulsive force calculations in swimming frogs. I. A momentum-impulse approach. *J. Exp. Biol.* **208**, 1435-1443.

Peng, J. and Dabiri, J. O. (2007). A potential flow, deformable-body model for fluid-structure interactions with compact vorticity: application to animal swimming measurements. *Exp. Fluids* **43**, 655-664.

Peng, J., Dabiri, J. O., Madden, P. G. and Lauder, G. V. (2007). Non-invasive measurement of instantaneous forces during aquatic locomotion: a case study of the bluegill sunfish pectoral fin. *J. Exp. Biol.* **210**, 685-698.

Pereira, F., Gharib, M., Modarress, M. and Dabiri, D. (2000). Defocusing DPIV: a 3-component 3-D DPIV measurement technique, application to bubbly flows. *Exp. Fluids* **29**, S78-S84.

Provenzale, A. (1999). Transport by coherent barotropic vortices. *Annu. Rev. Fluid Mech.* **31**, 95-123.

Rosenhead, L. (1963). *Laminar Boundary Layer Theory*. Oxford: Oxford University Press.

Saffman, P. G. (1967). The self-propulsion of a deformable body in a perfect fluid. *J. Fluid Mech.* **28**, 385-389.

Saffman, P. G. (1992). *Vortex Dynamics*. Cambridge: Cambridge University Press.

Sane, S. P. (2003). The aerodynamics of insect flight. *J. Exp. Biol.* **206**, 4191-4208.

Schultz, W. W. and Webb, P. W. (2002). Power requirements of swimming: do new methods resolve old questions? *Integr. Comp. Biol.* **42**, 1018-1025.

Shadden, S. C. (2006). A dynamical systems approach to unsteady systems. PhD thesis, California Institute of Technology, USA.

Shadden, S. C., Lekien, F. and Marsden, J. E. (2005). Definition and properties of Lagrangian coherent structures from finite-time Lyapunov exponents in two-dimensional aperiodic flows. *Physica D* **212**, 271-304.

Shadden, S. C., Dabiri, J. O. and Marsden, J. E. (2006). Lagrangian analysis of entrained and detrained fluid in vortex rings. *Phys. Fluids* **18**, 047105.

Spedding, G. R., Rosen, M. and Hedenstrom, A. (2003). A family of vortex wakes generated by a thrush nightingale in free flight in a wind tunnel over its entire natural range of flight speeds. *J. Exp. Biol.* **206**, 2313-2344.

Stamhuis, E. J. and Nauwelaerts, S. (2005). Propulsive force calculations in swimming frogs. II. A vortex ring approach. *J. Exp. Biol.* **208**, 1445-1451.

Walker, J. A. (2004). Dynamics of pectoral fin rowing in a fish with an extreme rowing stroke: the threespine stickleback (*Gasterosteus aculeatus*). *J. Exp. Biol.* **207**, 1925-1939.

Warrick, D. R., Tobalske, B. W. and Powers, D. R. (2005). Aerodynamics of the hovering hummingbird. *Nature* **435**, 1094-1097.

White, F. (1991). *Viscous Fluid Flow* (2nd edn). New York: McGraw-Hill.

Wilga, C. D. and Lauder, G. V. (2004). Biomechanics: Hydrodynamic function of the shark's tail. *Nature* **430**, 850.

Willmott, A. P., Ellington, C. P. and Thomas, A. L. R. (1997). Flow visualization and unsteady aerodynamics in the flight of the hawkmoth *Manduca sexta*. *Philos. Trans. R. Soc. Lond. B Biol. Sci.* **352**, 303-316.